

Highly efficient CRISPR-mediated genome editing through microfluidic droplet cell mechanoporation

Received: 27 March 2024

Accepted: 11 September 2024

Published online: 16 September 2024

 Check for updatesYou-Jeong Kim^{1,2,7}, Dayoung Yun^{3,7}, Jungjoon K. Lee⁴, Cheulhee Jung³ ✉ & Aram J. Chung^{1,2,5,6} ✉

Clustered regularly interspaced short palindromic repeats (CRISPR)-based editing tools have transformed the landscape of genome editing. However, the absence of a robust and safe CRISPR delivery method continues to limit its potential for therapeutic applications. Despite the emergence of various methodologies aimed at addressing this challenge, issues regarding efficiency and editing operations persist. We introduce a microfluidic gene delivery system, called droplet cell pincher (DCP), designed for highly efficient and safe genome editing. This approach combines droplet microfluidics with cell mechanoporation, enabling encapsulation and controlled passage of cells and CRISPR systems through a microscale constriction. Discontinuities created in cell and nuclear membranes upon passage facilitate the rapid CRISPR-system internalization into the nucleus. We demonstrate the successful delivery of various macromolecules, including mRNAs (~98%) and plasmid DNAs (~91%), using this platform, underscoring the versatility of the DCP and leveraging it to achieve successful genome engineering through CRISPR–Cas9 delivery. Our platform outperforms electroporation, the current state-of-the-art method, in three key areas: single knockouts (~6.5-fold), double knockouts (~3.8-fold), and knock-ins (~3.8-fold). These results highlight the potential of our platform as a next-generation tool for CRISPR engineering, with implications for clinical and biological cell-based research.

Genome editing has transformed biological research by enabling precise modifications to the genomes of various organisms, especially those of living cells¹. This capability has allowed scientists to manipulate innate genetic functions, to their specific objectives, with unprecedented accuracy. Key genome editing technologies include zinc-finger nucleases (ZFNs), transcription activator-like effector nucleases (TALENs), and the clustered regularly interspaced short palindromic repeats (CRISPR)–Cas9 system². Notably, the CRISPR–Cas9 system has garnered significant attention due to its

simplicity, versatility, and high efficiency in genome manipulation, paving the way for complex and precise genomic engineering³. It should be mentioned that the efficacy of CRISPR as a therapeutic modality is contingent upon the successful internalization of the CRISPR systems into the targeted cells. This highlights the importance of developing a suitable delivery method and specifying the structural/morphological format of the CRISPR systems for optimal therapeutic outcomes. CRISPR-associated complexes can be delivered in various forms, including plasmid DNAs (pDNA), mRNAs encoding the Cas9

¹Department of Bioengineering, Korea University, Seoul, Republic of Korea. ²Interdisciplinary Program in Precision Public Health (PPH), Korea University, Seoul, Republic of Korea. ³Department of Biotechnology, Korea University, Seoul, Republic of Korea. ⁴Department of Biochemistry, National University of Singapore, Singapore, Singapore. ⁵School of Biomedical Engineering, Korea University, Seoul, Republic of Korea. ⁶MxT Biotech, Seoul, Republic of Korea. ⁷These authors contributed equally: You-Jeong Kim, Dayoung Yun. ✉ e-mail: damo363@korea.ac.kr; ac467@korea.ac.kr

protein and single-guide RNAs (sgRNA), as well as ribonucleoprotein (RNP) complexes, which involve the fusion of sgRNA with the Cas9 protein⁴. Characterized by its stability and cost-effective large-scale production in laboratory settings, pDNA is a versatile molecular entity. Although its stability contributes to enhanced efficiency, it carries the risk of undesired prolonged expression of Cas9 and sgRNA, potentially increasing the probability of off-target effects^{5,6}. Furthermore, transfection utilizing plasmids has been documented to induce cell death in specific cell types, including embryonic stem cells^{6,7}. In contrast, mRNA delivery expedites the gene editing process, as transcription is not required⁸. Although mRNA has the advantage of reducing the chances of unintended genetic modifications when compared with that in pDNA, its low stability renders it susceptible to rapid degradation, reducing the editing efficiency. As an alternative, RNP has garnered widespread adoption as the preferred delivery format for the CRISPR–Cas9 engineering. Introducing RNP into the cells establishes a state ready for CRISPR activity, circumventing the transcription and translation processes required by other delivery forms, thereby enabling rapid editing⁴. In contrast to pDNA, RNP exhibits a relatively short lifespan, mitigating the risks associated with off-target editing⁹. Furthermore, RNP ensures greater stability against degradation when compared with that achieved with the mRNA delivery form^{6,10}. Although delivering the CRISPR–Cas9 system as RNP offers numerous advantages, the internalization process has certain challenges, mainly due to the considerable size of the Cas9 protein (approximately 160 kDa), which necessitates delivery into the nucleus. Therefore, selection of an appropriate delivery method is of paramount importance¹¹.

To facilitate effective RNP delivery for CRISPR-mediated applications, delivery strategies such as lipofection^{12,13}, electroporation^{14,15}, and cell-penetrating peptide¹⁶ are commonly employed. Electroporation is predominantly used because of its operational simplicity and relatively high editing efficiency. It is a technique that creates transient nanopores in the cell membrane through electrical pulses, allowing the passage of biomolecules via electrophoretic migration¹⁷. This method has been demonstrated to be effective across a range of cell types. However, a notable drawback of electroporation is its dependence on high-voltage electrical pulses, which can result in substantial cell death and modulation of gene expression. Furthermore, reports indicate that electroporation alone often induces unintended DNA double-strand breaks, which significantly limits its potential for genomic editing applications¹⁸.

To address these limitations, several microfluidic platforms have been proposed to provide enhanced efficiency, consistency, stability, and throughput, along with reduced reagent consumption^{19–21}. For example, microfluidic mechanoporation, using fluid–cell–structure interactions, has been utilized for RNP delivery. Deng et al. reported an inertial, microfluidic cell hydroperator, which enabled cell elongation to create discontinuities in the cell membrane. Successful editing of the COL1A1 gene in A2780cis cells²² was demonstrated; however, the wedge-shaped design is susceptible to channel clogging. Another example is constriction-based microfluidic intracellular delivery, known as cell squeezing^{23–25}. This platform passes cells through a series of narrow constrictions, allowing the delivery of biomolecules including mRNA and RNPs into different cell types. Since the delivery relies solely on the passive diffusion of RNPs into cells, a limited knockout efficiency via non-homologous end joining (NHEJ) was reported²³. In addition, it has been documented that this diffusion-based method fails to perforate the nuclear envelope, preventing pDNA-based transfection²⁶. Therefore, additional demonstrations and validations, such as pDNA transfection, highly effective knockout, large deletions through multiplexed knockouts, and gene insertion (knock-in via homology-directed repair (HDR)) are warranted. Furthermore, a newly developed method must exceed the capability and scalability of electroporation, which is the current standard for gene editing.

Here, we present a microfluidic platform called the droplet cell pincher (DCP), designed as a highly efficient and safe CRISPR-mediated genome editing tool. Our approach integrates droplet microfluidics with cell mechanoporation, allowing the encapsulation and controlled passage of cells and CRISPR–Cas9 RNPs through a microscale constriction. This process results in the creation of discontinuities in both the cell and nuclear membranes, facilitating the internalization of CRISPR–Cas9 RNPs into the nucleus. We demonstrated that this platform could be used for the delivery of diverse macromolecules, including mRNAs and pDNAs, underscoring the versatility of the DCP. Next, the DCP platform was successfully employed to perform various genome editing operations, including single knockouts, double knockouts, and single knock-ins. Notably, the editing efficiency surpassed that of electroporation, firmly validating its potential as a highly efficient gene editing tool.

Results and discussion

Device characterization

The DCP platform operates on the principle of droplet cell mechanoporation, integrating droplet microfluidics with physical cell permeabilization. Recently, we introduced a droplet cell squeezing method involving the passage of droplets containing cells through a series of narrow constrictions²⁷. Although the system exhibited high transfection/delivery performance in delivering various biomolecules and cell types, it often experienced channel clogging due to the presence of multiple constrictions and slow droplet passage speed. Furthermore, this method demonstrated suboptimal gene delivery outcomes, limiting its applicability to genomic engineering, particularly in CRISPR-mediated applications. A high flow-rate operation is an option to overcome these challenges; however, such flow conditions compromise stable droplet generation and cell encapsulation upstream. Therefore, we hypothesized that these problems could be fundamentally resolved by separately achieving stable droplet generation upstream and subsequently passing the droplets through a single constriction at a high speed downstream. Our redesigned platform not only enhances throughput and addresses clogging issues while preserving cell viability but also significantly improves delivery and transfection efficiency. This demonstrates that the proposed platform is capable of achieving various highly efficient CRISPR-mediated genome editing tasks that have not been accomplished before.

To this end, we designed a DCP platform presented in Fig. 1a, b and Supplementary Movie 1. The cell suspension, mixed with the target biomolecules (e.g., CRISPR–Cas9 systems) and oil for droplet generation, was pumped independently into the microchannel using conventional syringe pumps. The microfluidic flow-focusing geometry facilitated the generation of uniform droplets, allowing stable droplet formation and upstream cell and biomolecule encapsulation. The generated droplets were accelerated by injecting an additional oil sheath flow. The accelerated droplets containing cells and biomolecules were then rapidly guided through a single constriction, inducing transient permeabilization of the membrane (Fig. 1c and Supplementary Movie 2). This high-speed cell mechanoporation process allows the convective internalization of external biomolecules into both the cytosol and nucleus through secondary flows developed in droplets, a capability that conventional cell squeezing methods, which rely solely on diffusion, do not possess. It should be noted that additional oil injection does not require additional biomolecules, and any excessive oil is fully recycled owing to the immiscibility and density difference between the two phases. Moreover, adopting a single constriction with a high-speed droplet passage substantially decreases the risk of channel clogging.

To validate the effectiveness of the DCP in internalizing the biomolecules into cells, we first attempted to deliver 0.3 mg/mL of 3–5 kDa fluorescein isothiocyanate (FITC)-conjugated dextran (FITC-

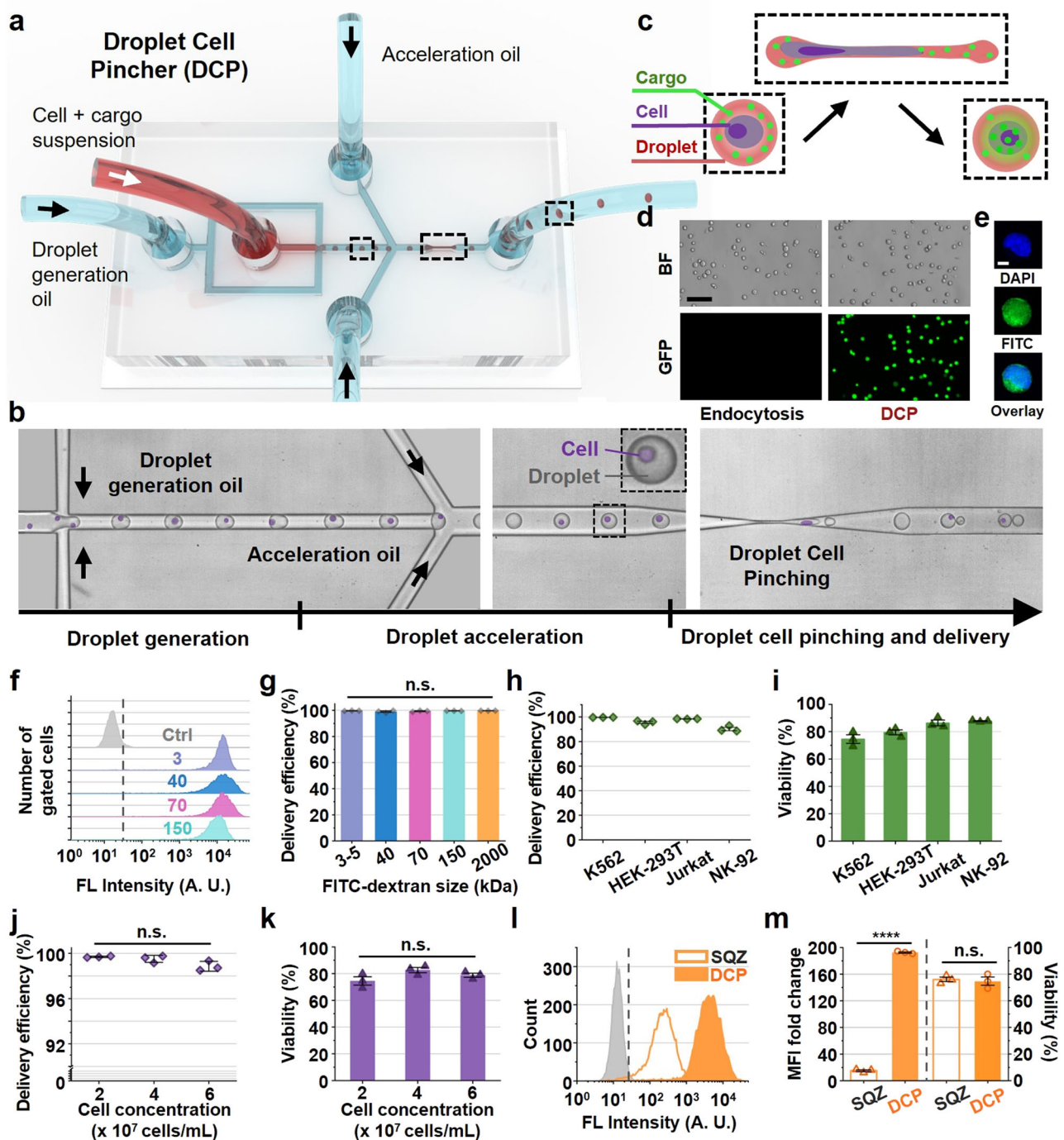


Fig. 1 | Overview of the droplet cell pincher (DCP) platform and delivery characterization. **a** Schematic representation of DCP. **b** High-speed microscope images demonstrating stable droplet generation with cell encapsulation, droplet acceleration through additional sheath flow, and droplet cell-pinching process. **c** Detailed illustration of the intracellular-delivery mechanism through droplet cell mechanoporation, encompassing encapsulation, pinching and transient cell deformation, and internalization. **d** Bright-field (BF) and fluorescence (FL) images showing the delivery of 3–5 kDa fluorescein isothiocyanate (FITC)-dextran into K562 cells via DCP (scale bar: 200 μm). **e** Confocal images of a K562 cell (scale bar: 5 μm). **f** Fluorescence intensity histograms and **g** Delivery efficiency of different FITC-dextran sizes into K562 cells. **h** 2000 kDa FITC-dextran delivery efficiency, and **i** Cell

viability for various cell types. **j** 2000 kDa FITC-dextran delivery efficiency and **k** Cell viability as a function of cell concentration. **l** Plots of fluorescence intensity histograms, and **m** MFI fold change and cell viability for cell squeezing (SQZ) and DCP. All bars indicate mean \pm standard error of the mean ($N=3$ biological replicates). Each data point is based on flow cytometry analysis performed independently on different cell flasks. n.s. stands for no statistical difference; *, **, ***, and **** indicate P values below 0.05, 0.01, 0.001, and 0.0001, respectively. Statistical analyses were performed using one-way ANOVA and Tukey's post-hoc tests for multiple comparisons. Source data are provided as a source data file. Detailed P values are provided in the source data file.

dextran) into the K562 cells. FITC-dextran was specifically selected for its size variety, strong fluorescence, and minimal cell surface-binding characteristics attributed to its negative surface charge²⁸. For evaluating the FITC-dextran delivery after processing the cells via the DCP,

imaging of the K562 cells was conducted 18 h post-delivery. As shown in Fig. 1d, e, strong and uniform fluorescence signals were observed in the cytosol and nucleus. In contrast, the endocytosis group (positive control), comprising cells co-incubated with FITC-dextran during the

DCP process, exhibited no detectable fluorescence, validating the success of the DCP-induced FITC-dextran delivery.

Next, we investigated the delivery dependence of the DCP platform on the cargo size. We postulated that a single yet rapid cell mechanoporation process could facilitate the effective internalization of large dextrans. To validate this, different molecular weights of 3–2000 kDa FITC-dextran, equivalent to a size range of approximately 3–50 nm, were delivered into the K562 cells under optimized fluidic and geometric conditions (a detailed description of the optimized parameters is presented in the next section). For quantitative characterization, we conducted a flow cytometry-based analysis. As shown in Fig. 1f, g, nearly 100% delivery efficiency was consistently achieved, regardless of the dextran size.

Additionally, we evaluated the effect of the cell type on the delivery efficiency. Under the same experimental conditions, 2000 kDa FITC-dextran was internalized into each cell type at the same concentration (0.3 mg/mL), with cell density of 2×10^7 cells/mL. The results depicted in Fig. 1h, i, consistently demonstrate highly efficient delivery exceeding 90%, with concurrent preservation of the cell viability at levels higher than 75% across all tested cell types. The fold changes in the mean fluorescence intensity (MFI) are plotted separately in Supplementary Fig. 1. All these results highlight that the DCP platform can be used for both suspension and adherent cells in various delivery applications.

Next, we assessed the scalability of the DCP platform by evaluating the delivery efficiency as a function of the cell concentration. This investigation is crucial because high scalability should be guaranteed for an intracellular delivery platform to be used in cell-based therapy. For example, the production of ex vivo CAR-T cells for patient reinfusion requires approximately 1×10^8 cells per kg of body weight, indicating the necessity for high-throughput processing²⁹. With the DCP, we can routinely process 2×10^7 cells/mL, a notably higher density than that possible with existing microfluidic platforms, which typically operate within the range of 10^5 – 10^7 cells/mL^{26–28,30–32}. At increased cell concentrations, the platform exhibited stable performance without compromising the delivery efficiency and viability, achieving levels as high as 6×10^7 cells/mL, as shown in Fig. 1j, k (refer to Supplementary Fig. 2 for MFI values). As the platform operates continuously with channel parallelization, it is expected to meet the increased scalability demands for cell-based therapeutic applications.

To characterize the performance of the DCP platform in comparison with that of the representative microfluidic delivery method, namely, cell squeezing²⁸, under identical operational conditions, we delivered equivalent quantities of cargo (2000 kDa FITC-dextran) into the K562 cells. As illustrated in Fig. 1l, m, both scenarios (with and without the use of droplets) exhibited effective dextran delivery (see Supplementary Fig. 3 for the delivery efficiency) and no discernible differences in viability; nevertheless, a significant MFI fold change was evident in the DCP method (192.7-fold) when compared with that in cell squeezing (15.1-fold). Substantially higher delivery performance of the DCP platform was observed, which could be attributed to the effective concentration of dextran and secondary flows in droplets which enhance convective transport of cargo into cells²⁷. Considering that the DCP microchannel is mostly filled with oil, the use of droplets decreases the aqueous volume; therefore, even with an equivalent amount of analytes, the cells are exposed to an environment with a higher concentration than that in cell squeezing (see Supplementary Fig. 4). Collectively, these results suggest that our DCP platform is a competitive solution with superior delivery and minimal analyte consumption.

Optimization of device operation

Delivery efficiency is critically influenced by the operational conditions, specifically the fluidic and geometric parameters, as illustrated in Fig. 2a. To identify the optimized operational conditions, our

investigation initially focused on assessing the effects of the flow conditions on delivery efficiency, MFI fold change, and cell viability. The upstream flow condition was fixed for stable droplet generation and encapsulation³³, and the cell density (2×10^7 cells/mL) and FITC-dextran size and concentration (2000 kDa and 0.3 mg/mL, respectively) were set identically. Under these circumstances, we first attempted to internalize dextran into the K562 cells with different oil sheath flow rates while utilizing the same microfluidic channel geometry with a width of 8 μ m and length of 70 μ m. The downstream oil sheath flow rate was systematically increased from 0 to 1.5 mL/h in increments of 0.5 mL/h. Subsequently, we calculated the corresponding delivery efficiency, MFI fold change, and cell viability. As depicted in Fig. 2b, nearly 100% delivery efficiency was achieved at all flow rates, including the case with no oil sheath fluid. For a comprehensive comparison of the delivery performance, MFI fold changes were calculated relative to those in the control group and the results are presented in Fig. 2c. The introduction of oil sheath fluids resulted in a significant increase in the MFI change. Broadly speaking, a higher oil sheath flow rate resulted in an increased MFI fold change; however, a decrease in MFI was observed as the flow rate was further elevated to 1.5 mL/h. Concurrently, the viability exhibited a monotonous decrease with increasing oil sheath flow rate; a substantial decrease in viability was observed at 1.5 mL/h (Fig. 2d). Considering both aspects, it is postulated that at the highest oil sheath flow rate, excessive cell deformation is induced beyond the self-repairing capacity of the cell (i.e., membrane resealing), resulting in a diminished MFI fold change.

To determine the optimal flow conditions for effective cargo delivery, we evaluated a new metric, defined as the product of the MFI fold change and cell viability. This metric serves as a practical measure of the net intracellular delivery of biomolecules, assuming both MFI fold change and viability are presented simultaneously. The calculated values for each tested flow rate of the oil sheath fluid were 117.8, 130.2, 143.7, and 110 (A.U.). Upon careful consideration of these calculations, a sheath fluid flow rate of 1.0 mL/h was identified as the optimal condition that maximizes the delivery efficiency while concurrently preserving the cell viability.

Subsequently, we investigated the influence of the geometric parameters of the microchannel on the overall delivery level and cell viability. As previously noted, a single constriction was employed to avoid potential clogging; therefore, we investigated two primary factors: the constriction (i.e., gap) width and length. Initially, three different constriction gap widths of 6, 8, and 10 μ m were evaluated while maintaining a constant constriction length of 70 μ m and sheath flow rate of 1.0 mL/h. As illustrated in Fig. 2e, f, close to 100% delivery efficiency was attained in delivering 2000 kDa FITC-dextran into the K562 cells; however, the MFI fold change decreased as the channel gap width increased. As expected, a reduction in cell viability was observed with decreasing gap width, as shown in Fig. 2g. The application of the metric describing the net intracellular delivery indicated that a constriction width of 8 μ m was optimal.

We also examined the effect of the constriction length on dextran internalization into the K562 cells. The constriction length was varied from 40 to 100 μ m, with a constant gap width of 8 μ m and sheath flow rate of 1.0 mL/h while keeping other parameters unchanged. The width of 8 μ m provides a sufficiently narrow gap for pinching the K562 cells; thus, it was observed that the delivery efficiency exceeded 99% across all cases, as shown in Fig. 2h. We hypothesized that increasing the constriction length would enhance the intracellular delivery level, potentially leading to reduced cell viability. As anticipated, the longest pinching length of 100 μ m resulted in the largest fold change in MFI of 307.47 (Fig. 2i). However, this enhancement in the MFI fold change was accompanied by the lowest viability of 36.8%, as shown in Fig. 2j. Furthermore, only a slight difference was observed in both the MFI fold change and viability ($p < 0.5$) at the pinching lengths of 40 and 70 μ m. We postulated that the relatively short constriction lengths of 40 and

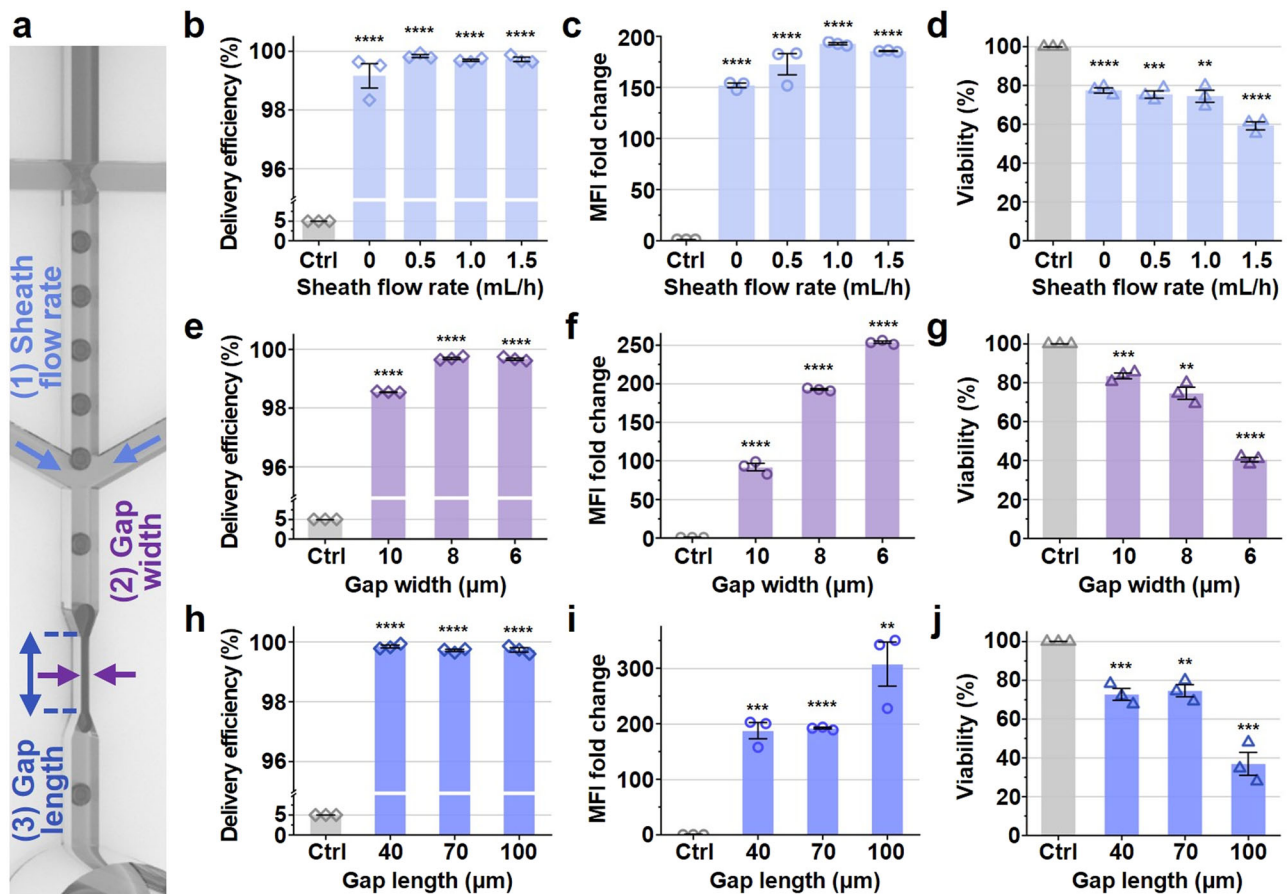


Fig. 2 | Delivery characterization by 2000 kDa FITC-dextran delivery into K562 cells at different operational flow and geometric conditions. **a** Parameters of the DCP platform determining performance. Delivery efficiency, MFI fold change, and viability for different **b–d** sheath flow rates, **e–g** gap widths, and **h–j** gap lengths. All bars indicate mean \pm standard error of the mean ($N=3$ biological replicates). Each

data point is based on flow cytometry analysis performed independently on different cell flasks. n.s. stands for no statistical difference; *, **, ***, and **** indicate P values below 0.05, 0.01, 0.001, and 0.0001, respectively. Statistical analyses were performed using one-way ANOVA and Tukey's post-hoc tests for multiple comparisons. Source data and detailed P values are provided in the source data file.

70 μm may not allow for maximal cell deformation, thus explaining the subtle differences. Nevertheless, when evaluating the product of the MFI fold change and viability, the pinching length of 70 μm was identified as the most suitable dimension.

In summary, for the delivery of 2000 kDa FITC-dextran into K562 cells, the optimal conditions were determined to be a flow rate of 1.0 mL/h, constriction width of 8 μm , and pinching length of 70 μm . These optimized conditions were employed for various biomolecule delivery experiments, as described in the subsequent sections.

Intracellular delivery of functional biomolecules through DCP

To assess the versatility of the DCP platform beyond its application to FITC-dextran delivery, we aimed to internalize functional biomolecules, such as eGFP-encoded mRNA and GFP-encoded pDNA, into the K562 cells. Transfection efficiency and cellular viability were investigated using the optimized operational conditions identified above. First, a 2 $\mu\text{g}/\text{mL}$ of 996-nucleotide eGFP-mRNA construct was internalized into the K562 cells using the DCP platform, with varying mRNA concentrations. As shown in Fig. 3a and Supplementary Fig. 5a, uniform and strong fluorescent signals were observed only in the cells treated with the DCP platform, whereas negligible fluorescence was detected in the positive control.

To quantify the transfection efficiency based on the mRNA concentration, 0.2, 2, and 20 $\mu\text{g}/\text{mL}$ of mRNA were internalized using the DCP under the optimized delivery conditions (see Methods for more details). Subsequently, flow cytometry analysis, presented in Fig. 3b

(with $N_{\text{cell}}=5000$), was used to systematically measure the signal from each cell. The corresponding MFI fold changes are presented separately in Fig. 3c. At a concentration of 2 $\mu\text{g}/\text{mL}$, a transfection efficiency of ~99% and a 47-fold change in the MFI were achieved; the highest concentration resulted in a 726.1-fold change in the MFI. Notably, this transfection performance surpassed that of previously reported microfluidics-based mRNA transfection results based on substantially higher mRNA consumption and concentrations^{27,30,31,34,35}.

Next, we prepared the GFP-encoding pDNAs of various sizes ranging from 4.1–9.1 kbp for delivery into the K562 cells. In contrast to mRNA, the transfection of cells with pDNA presents a greater challenge, as pDNA must pass not only through the cellular membrane but also navigate through the nuclear envelope. Moreover, owing to its distinctive morphological shape and larger molecular footprint, successful pDNA delivery presents a notably greater complexity. We hypothesized that the DCP platform can facilitate pDNA cell transfection. To validate this, 7.9 kbp pDNA was first internalized into the K562 cells. As depicted in Fig. 3d and Supplementary Fig. 5b, cells treated with the DCP platform exhibited high fluorescence intensity, indicating successful transfection. At a concentration of 50 $\mu\text{g}/\text{mL}$, the transfection efficiency was evaluated for different pDNA sizes, as shown in Fig. 3e. As anticipated, larger pDNA sizes posed greater challenges for internalization, resulting in a relatively lower transfection efficiency. However, it should be noted that conventional microfluidic platforms, which rely on cell squeezing, fail to demonstrate pDNA-based transfection^{26,28}; therefore, the DCP

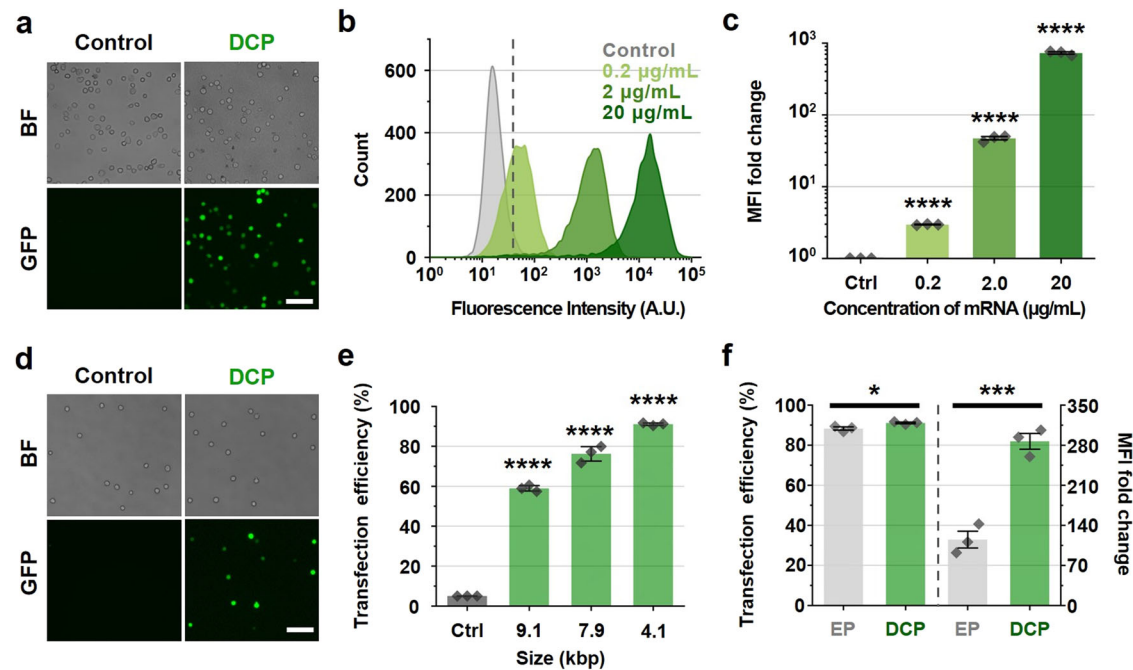


Fig. 3 | mRNA and plasmid DNA cell transfection using the DCP platform.

a Bright-field and fluorescence images showing 2.0 µg/mL of eGFP-mRNA expression via endocytosis and DCP after 24 h. **b** Fluorescence intensity histograms, and **c** MFI fold change of mRNA expression as a function of mRNA concentration. **d** Bright-field and fluorescence images depicting the transfection of 50 µg/mL of GFP-encoding pDNA with a size of 7.9 kbp. **e** pDNA transfection efficiency of K562 cells with different pDNA sizes. **f** Comparison of transfection efficiency and MFI fold

change for DCP and electroporation (EP). All bars indicate mean \pm standard error of the mean ($N=3$ biological replicates). Each data point is based on flow cytometry analysis performed independently on different cell flasks. n.s. stands for no statistical difference; *, **, ***, and **** indicate the P values below 0.05, 0.01, 0.001, and 0.0001, respectively. Statistical analyses were performed using one-way ANOVA. Source data are provided as a source data file. Detailed P values are provided in the source data file.

platform exhibits significant potential for application to DNA-mediated engineering.

To assess the performance in comparison with that of electroporation, we tested 4.1 kbp pDNA transfection using a concentration of 50 µg/mL while maintaining the same cell concentration for each method. While both methods appear to have similar transfection efficiencies, as shown in Fig. 3f (with the DCP method statistically exhibiting superior transfection efficiency), the MFI fold change revealed clear distinctions between the two approaches. Specifically, the DCP method achieved an approximately 286.7-fold increase, surpassing that of electroporation, which resulted in an approximately 115-fold increase. In addition to comparing the transfection performance, we analyzed the changes in the cell shape following treatment with DCP and electroporation. Given the documented evidence that the cell mechanoporation process has superior capability to preserve the cell functionality and stability than electroporation³⁶, our objective was to directly compare the alterations in the cell morphological phenotype after treatment. As can be seen in Supplementary Fig. 6, we confirmed that electroporation induced more significant alterations, consistent with previous findings³⁵. In short, these differences clearly highlight that the DCP platform is a superior and safer alternative than electroporation.

CRISPR–Cas9-mediated genome editing

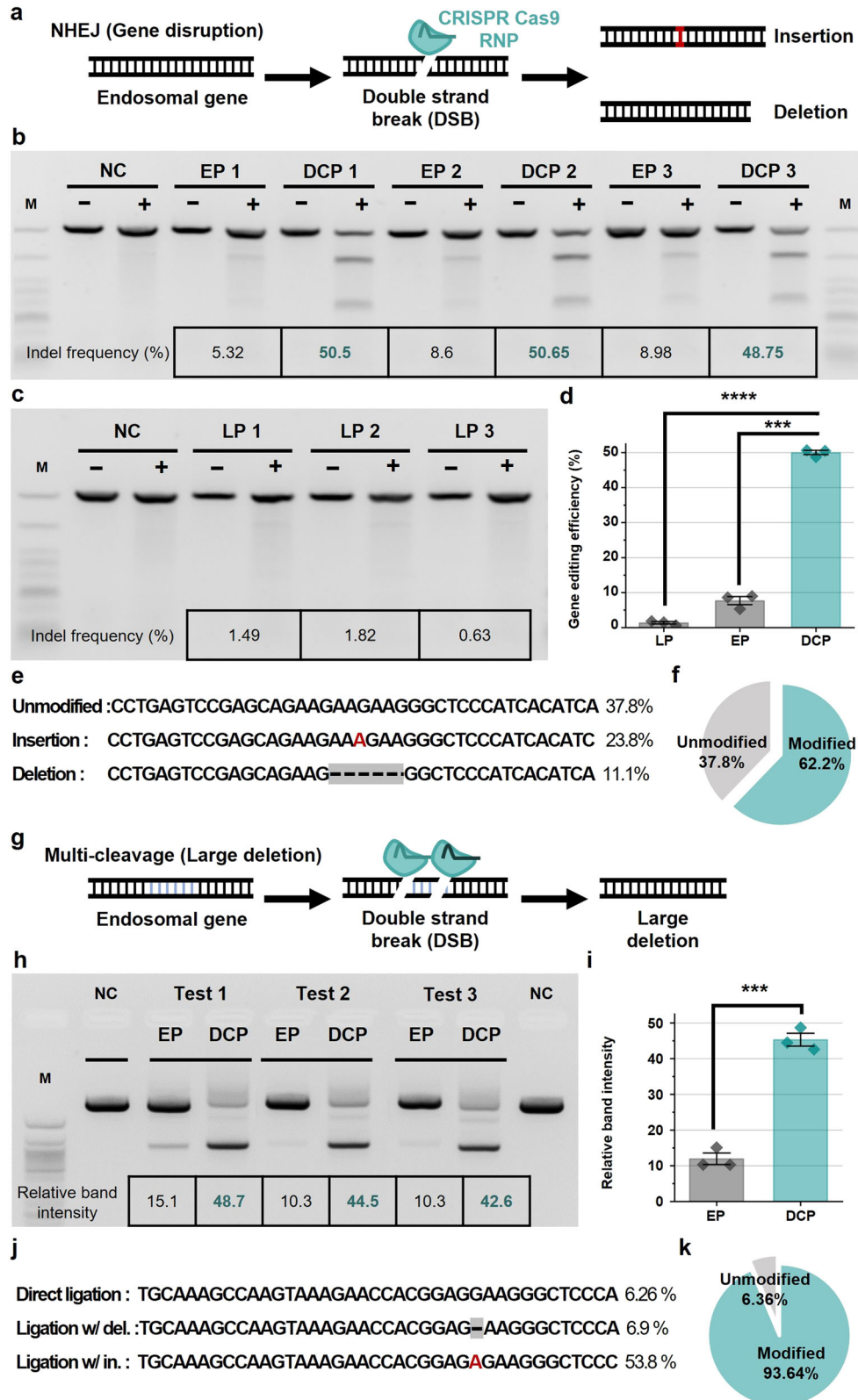
The sgRNA guides Cas9 to the targeted DNA sequence, creating double-strand breaks (DSBs). Subsequently, two primary repair mechanisms are activated, NHEJ and HDR³⁷. As illustrated in Fig. 4a, NHEJ repairs the DSBs by directly rejoining the ends, often resulting in small insertion and deletion mutations (indels). In contrast, the HDR mechanisms facilitate precise insertion of a foreign genetic sequence at a specific genomic locus. This process involves the utilization of external DNA or RNA sequences introduced alongside the

CRISPR–Cas9 complex, which serves as a template for the precise integration of genetic material at the designated genomic site (see Fig. 5a).

We hypothesized that our DCP platform could effectively facilitate both NHEJ for knockout and HDR for knock-in applications. By employing the optimized operational conditions, we attempted to deliver the CRISPR–Cas9 RNPs at a concentration of 100 µg/mL into the K562 cells, targeting the *EMX1* locus (see the Methods section for more details). The CRISPR–Cas9 RNP complex was prepared and directly delivered into the cells through the DCP while ensuring a uniform cell density of 2×10^7 cells/mL in all the experiments. Note that genomic editing can only be achieved if the RNP complex is localized in the nucleus. Following the delivery of the RNPs into the cells, the cells were collected after 72 h of incubation, providing sufficient time for the RNPs to engage and induce NHEJ or HDR within the nucleus. Subsequently, for editing efficiency characterization, the cells were harvested to extract the DNA. For a direct one-to-one comparison with other benchtop methods, including electroporation (EP) and lipofection (LP) (Figs. 4 and 5), we consistently employed the same experimental conditions unless specified otherwise.

The *EMX1* knockout efficiency was evaluated using the T7E1 assay, which is known for its effectiveness in detecting indels greater than 1 nt in length³⁸. As shown in Fig. 4b–d, the analysis of the average band intensities indicated an indel frequency of 1.3% for lipofection, 7.6% for electroporation, and over 50% for DCP, thereby demonstrating an editing frequency approximately twenty times greater than that of lipofection and efficiency approximately five times higher than that of electroporation.

To precisely validate the successful occurrence of indels at the target loci facilitated by the DCP, we conducted next-generation sequencing (NGS), specifically focusing on indels within 50 base pairs from the target site (Fig. 4e, f). Among the reads with no modification,



37.84% (3,227,127 reads) were identified, whereas the remaining reads exhibited evident indel events, accounting for 62.16% knockout editing efficiency (slightly higher than that in the T7E1 analysis). Notably, the most prevalent alteration involved adenine insertions, accounting for 23.8% (2,025,764 reads), followed by 11.1% (951,250 reads), which were characterized by deletions of six nucleotide sequences (Supplementary Fig. 7a).

Next, we assumed that the DCP platform could generate dual cleavage by facilitating the delivery of two distinct CRISPR–Cas9 RNPs into the nucleus, thereby enabling multiplexed genome editing, as illustrated in Fig. 4g. The assessment of multiplexed NHEJ efficiency was conducted through the internalization of two separate RNP complexes, each with a concentration of 50 μg/mL. Two distinct loci within *EMXI* were targeted and delivery was achieved using the DCP

Fig. 4 | Various genome editing via CRISPR–Cas9 ribonucleoprotein (RNP) delivery into K562 cells followed by subsequent editing efficiency characterization through the NHEJ pathway at the targeted site(s). **a** Schematic of NHEJ repair pathway. Percentage of indel formation verified by T7E1 assay using **b** Electroporation (EP), DCP, and **c** Lipofection (LP). **d** Editing efficiency of each method. **e** PCR product sequencing data for the *EMXI* targeting region in K562 cells. Representative sequences for indels. The inserted sequence is highlighted in red, and the deletions are denoted by the gray box. **f** Ratio between unmodified and modified genes quantified using next-generation sequencing (NGS). **g** Schematic of the dual-DSB approach and ligation. **h** Bands representing the amplified multiplex products using electroporation and DCP for comparison. A 50 bp DNA ladder (left,

NEB N3236S) and a 1 kb DNA ladder (right, NEB N3232S) were used as size markers. **i** Relative band intensity of EP and DCP. **j** PCR product sequencing data for the *EMXI* targeting region. Representative sequences for large deletions (with or without indels). **k** Ratio between unmodified and modified genes quantified using NGS. All bars indicate mean ± standard error of the mean (*N* = 3 biological replicates). Each data point is based on gel image analysis performed independently on different cell flasks. n.s. stands for no statistical difference; *, **, ***, and **** indicate *P* values below 0.05, 0.01, 0.001, and 0.0001, respectively. Statistical analyses were performed using one-way ANOVA. Source data and detailed *P* values are provided as the source data file.

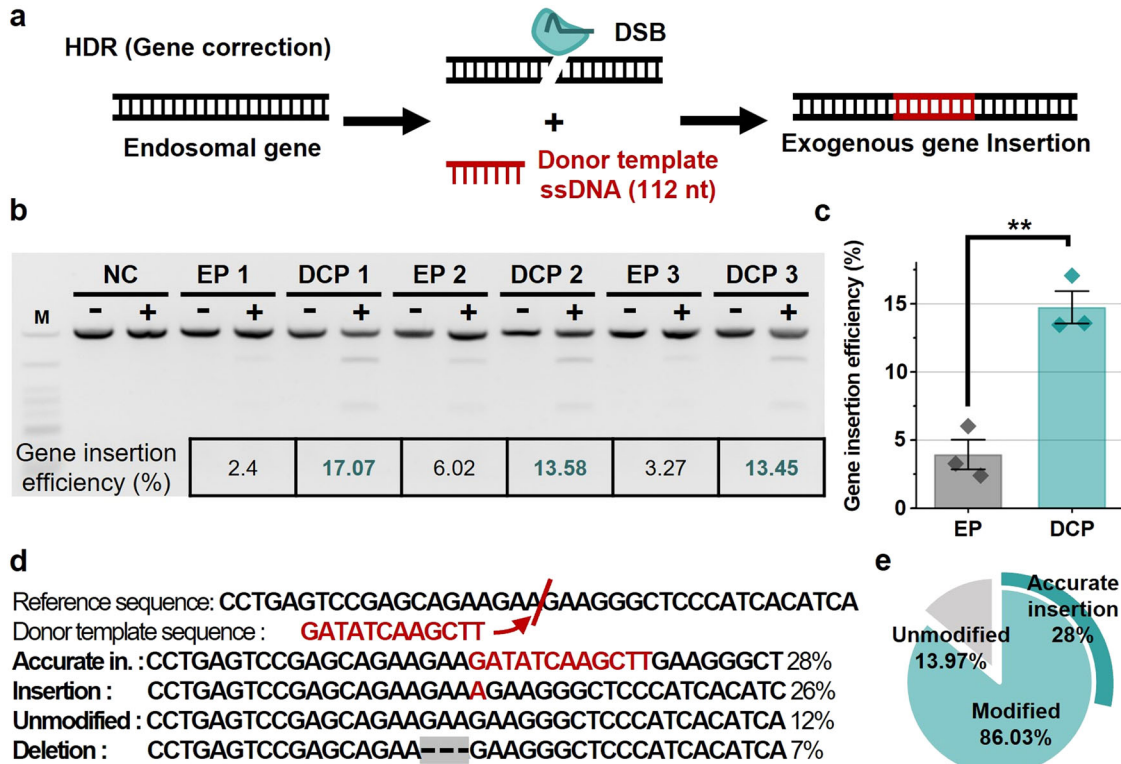


Fig. 5 | Genome editing via CRISPR–Cas9 RNP delivery into K562 cells and subsequent editing efficiency characterization via the HDR pathway at the targeted site(s). **a** Schematic of the HDR repair pathway. **b** Restriction enzyme (RE)-cleaved PCR products indicative of HDR. **c** Quantification of HDR frequency targeting *EMXI* in K562 cells. **d** Representative sequences for accurate insertion of donor-template sequences and other indels. **e** Ratio between unmodified and modified genes, including those with accurate insertion, quantified using NGS. All

bars indicate mean ± standard error of the mean (*N* = 3 biological replicates). Each data point is based on gel image analysis (RE assay) performed independently on different cell flasks. n.s. stands for no statistical difference; *, **, ***, and **** indicate *P* values below 0.05, 0.01, 0.001, and 0.0001, respectively. Statistical analyses were performed using one-way ANOVA. Source data are provided as a source data file. Detailed *P* values are provided in the source data file.

platform and an electroporator. Lipofection was excluded owing to its inferior editing efficiency (Fig. 4c, d) in the single RNP editing trials. Following the induction of DSBs at the designated sites, deletions were observed within the genomic sequences located between the targeted loci. Subsequent ligation mechanisms were activated to repair the genomic remnants resulting from the induced DSBs. Multiplexing efficiency was indirectly evaluated by quantifying the amplification of the cleaved region using polymerase chain reaction (PCR) primers. The primers were designed to amplify a 2069 bp segment encompassing the wild-type target site, which facilitated the detection of bands at the specified “NC” location. The induction of two DSBs led to the targeted deletion of a sizable genomic fragment measuring 1355 bp, as intended (Fig. 4h). Consequently, a 714 bp residual fragment emerged, which was attributable to either direct ligation or potentially small-scale deletions and insertions. Gel electrophoresis of the PCR amplicons revealed distinct bands, confirming successful genome editing at the anticipated 714 bp location. The identification of small-scale insertions

and deletions based on band patterns posed a challenge, whereas larger-scale insertions were evident as smeared band patterns located prominently above the 714 bp threshold.

To assess the editing efficiencies of DCP and electroporation, the band intensities at the specific positions were analyzed for samples prepared using equivalent amounts of amplified genomic DNA (gDNA). The results indicated average values of 11.9 and 45.3 for electroporation and DCP, respectively (Fig. 4i). In comparison to electroporation, DCP demonstrated approximately 3.8-fold higher efficiency in achieving successful double knockouts, indicating its superior multiplexing editing efficiency over the current state-of-the-art method. Although agarose gel electrophoresis facilitated a qualitative comparison of the two platforms, quantifying the exact efficiencies of both CRISPR–Cas9 RNPs remained challenging. Therefore, NGS was employed to scrutinize the modifications within the target region (Fig. 4j, k). The analysis revealed that only 6.36% of the amplicons remained unmodified, whereas 93.64% exhibited various forms of

modification. Direct ligation following cleavage was observed in 6.26% of the cases. The remaining modifications encompassed various sizes of indels, with 6.9% sequence deletions and 53.8% sequence insertions (Supplementary Fig. 7b).

As another key example of genome editing, we demonstrated gene knock-in through HDR. It is worthwhile to mention that there are limited reports on knock-in demonstrations via microfluidics. Therefore, we hypothesized that our DCP platform is capable of effectively inserting genes at the desired locations. The initial objective was to deliver the same RNP targeting *EMX1*, accompanied by single-stranded DNA (ssDNA) serving as the HDR donor template (112 nt) (see Fig. 5a). This ssDNA template contained a sequence recognized by the restriction enzyme (RE), Eco-RV HF, which facilitates the convenient calculation of the insertion efficiency. Considering that gene insertion is conventionally less efficient than deletion, as reported in a previous study³⁹, we opted to increase the concentration of RNP two-fold during the delivery process.

When assessing the gene insertion efficiency by comparing the band intensities in gel electrophoresis and RE assay, electroporation demonstrated 3.9% efficiency, whereas DCP exhibited a significantly higher efficiency of 14.7%, yielding an approximately 3.8-fold increase in the insertion efficiency (Fig. 5b, c). Subsequently, NGS analysis was conducted to validate the precision of gene insertion (Supplementary Fig. 7c). The observed occurrences of various types of indel modifications within HDR accounted for 86.03%, as shown in Fig. 5d, e. Notably, instances where the donor template sequence was accurately inserted without indels and subsequently ligated comprised 28% of the outcomes, indicating that a significantly higher editing was achieved than that obtained from the RE assay. It is important to acknowledge that the HDR efficiency can be further improved by synchronizing and capturing cells in the S and G2 phases⁴⁰; therefore, we expect that the DCP platform has the potential to achieve even greater efficiency. Thus, this outcome underscores the immense potential of the DCP platform for diverse applications in genome editing, providing enhanced efficiency, safety, and cost-effectiveness compared to electroporation.

The genome editing process begins with internalization of the CRISPR–Cas system into the cells. However, the editing efficiency is constrained by the delivery method; this is recognized as a significant obstacle that prevents the realization of the full potential of the editing process. In this study, we developed a microfluidic gene delivery platform, which is a highly efficient genome editing tool capable of gene deletion and insertion along with multiplexing. Our current study primarily demonstrated genetic engineering using CRISPR–Cas9 systems. However, it is crucial to emphasize that the platform is adaptable to next-generation genome editing approaches, such as base editors⁴¹ and prime editors⁴². Given its capacity for facile macromolecule internalization, this platform holds considerable promise, particularly for prime editing, which involves proteins of substantial size (~240 kDa), albeit these are smaller than those tested in this study⁴³. Furthermore, our platform demonstrated highly effective mRNA and pDNA cell transfection, underscoring its versatility. In contrast to other microfluidic technologies, our platform leverages the unique secondary flows developed within droplets and employs highly rapid cell mechanoporation to achieve high levels of delivery. Most notably, a comparison with electroporation, which is the current standard for gene editing, indicated that the proposed platform outperforms electroporation in terms of both editing and transfection results. This confirmed the high potential of the DCP platform to establish a new standard for ex vivo genome editing. Additionally, as we previously mentioned, the DCP platform relies on cell mechanoporation for delivery; therefore, it is anticipated to achieve greater cell functionality and stability than electroporation³⁶.

While the DCP platform utilizes droplet microfluidics and requires an additional demulsification step for cell retrieval, this requirement can be effectively addressed through system automation, unlike with other microfluidic platforms^{31,44}. Nonetheless, the DCP platform distinguishes itself due to its near clog-free operation, high scalability, low analyte consumption, elevated editing/transfection efficiency, superior cell viability, and cost-effectiveness. In summary, we introduced a microfluidic platform for gene delivery that holds promise as a next-generation tool for CRISPR engineering, with significant implications for clinical and biological cell-based research.

Methods

Microfabrication

The microchannel mold was fabricated using conventional photolithography with an SU-8 photoresist (Microchem Corp., USA). Polydimethylsiloxane (PDMS Sylgard 184, USA) channels were replicated using standard soft lithography. The inlets and outlets were created by punching holes into the PDMS using a pin vise. Subsequently, oxygen-plasma treatment (CUTE, Femto Science, South Korea) was applied to bond the PDMS to a standard glass slide. The bonded chips underwent a baking process for a minimum of 24 h in a 75 °C oven, ensuring robust adhesion.

Cell culture

K562 (KCLN no.: 10243) and Jurkat (KCLN no.: 40152) cells were purchased from the Korean Cell Line Bank. HEK 293 T (Cat. no.: CRL-3216) cells were obtained from the ATCC. NK-92 cells were generously provided by the group associated with Professor J. Doh at Seoul National University (South Korea). The K562 and Jurkat cells were cultured according to the standard protocols in RPMI-1640 medium (Corning, USA) and supplemented with 10% fetal bovine serum (FBS; Gibco, USA) and 1% penicillin–streptomycin (Gibco, USA). HEK 293 T cells were cultured in DMEM with the same supplements. NK-92 cells were grown in an RPMI 1640 medium with L-glutamine (Corning, USA) supplemented with 10% FBS, 1% penicillin–streptomycin, and 100 U/ml IL-2 (PeproTech, USA). All cell types were incubated, maintained, and cultured at 37 °C with 5% CO₂.

Intracellular delivery procedure

The droplet generation oil (Bio-Rad, USA) was filtered using a 0.2 μm polytetrafluoroethylene syringe filter (Advantec, Taiwan). The cells were mixed with the target nanomaterials and loaded into 1–3 mL Luer-Lok plastic syringes (BD, USA). Opti-MEM (Thermo Fisher Scientific, USA) was used for 996 nt eGFP-mRNA (TriLink Biotechnologies, USA), pDNA, and CRISPR–Cas9 RNP delivery. FITC-dextran (3–2000 kDa; Sigma-Aldrich, USA) was resuspended in a complete cell medium at a concentration of 2×10^7 cells/mL. pCMV-T7-eGFP (4.119 kbp, BPK1098) pDNA (cat. No. 133962), 7.9 kbp pGreenPuro pDNA (cat. no. S1505A-1), and 9.1 kbp pDNA with the backbone vector pCDH-EF1-MCS-T2A-copGFP (System Biosciences, USA) were kindly provided by the laboratory under Professor S. Cho at Konkuk University (South Korea).

The sgRNA sequence was designed as 5' GAGTCCGAGCAGAA-GAAGAA 3' to target the *EMX1* (chromosome 2, 72933853 – 72933872, NCBI reference) site using chop-chop and Synthego (USA). For NHEJ demonstration, the Cas9 RNP complex was prepared using 30 μM endotoxin-free Cas9 protein, provided by Prof. J. Lee at NUS (Singapore), and 100 μM sgRNA purchased from Synthego. The 500 pmol RNP complex was formed by mixing the components at the same molar ratio for 10 min at room temperature in 1 mL Opti-MEM. In the case of NHEJ multiplexing, an additional sgRNA (5' AGTAAA-GAACCACGGAGTCA 3') targeting a different site of *EMX1* was used. Two types of RNP complexes, each consisting of 250 pmol, were prepared in separate tubes in 500 μL of Opti-MEM using the method mentioned above. For HDR, a 112 nt ssDNA donor template

(5' TACAAACGGCAGAAGCTGGAGGAGGAAGGGCCTGAGTCCGAGCAG AAGAAGATATCAAGCTTGAAGGCTCCCATCACATCAACCGTGGCC CATTGCCACGAAGCAGGCCA 3') containing the restriction enzyme site was utilized, purchased from Integrated DNA Technologies (IDT; USA). After preparing the RNP complex as described above, it was mixed with an equal amount of 500 pmol donor template and transfected into cells. During the experiments, the fluid flow was regulated using syringe pumps (Harvard Apparatus, USA). 1H,1H,2H,2H-Perfluoro-1-octanol (PFO, Thermo Fisher Scientific) was used to demulsify the droplets, allowing for cell retrieval. Subsequently, the collected cells were washed with Dulbecco's phosphate-buffered saline (DPBS; Modified, Hyclone, USA) and resuspended in the standard cell medium. Incubation durations of 18, 24, and 72 h were implemented for post-analysis of the delivery of FITC-dextran, nucleic acid transfection, and genome editing, respectively. Cell viability was assessed using a 0.4% trypan blue solution (Lonza, Switzerland).

Delivery efficiency calculation

Delivery or transfection efficiency is defined as the portion of the fluorescence signals surpassing the threshold, corresponding to the top 5% of fluorescence of the control group.

Electroporation and lipofection

The Neon transfection system (Thermo Fisher, USA) and CRISPRMAX reagent (CMAX00003, Invitrogen, USA) were used for electroporation and lipofection, respectively. The electroporation parameters, specifically those outlined in recipe #22 for K562 cells, were used according to the manufacturer protocol. Lipofection assays were performed according to the guidelines provided by the manufacturer.

Flow cytometry

The cells were harvested and suspended in DPBS for subsequent flow cytometry analyses. Flow cytometry was performed using a Guava EasyCyte flow cytometer from Luminex, USA. Cells of the control group were initially gated on their FSC and SSC to exclude debris and dead cells. The fluorescence of the gated cells was then measured using flow cytometry. An example of the flow cytometry gating scheme is provided in Supplementary Fig. 8.

DNA substrate construction and primer design

gDNA was extracted from the cell using the G-spin total DNA extraction kit (Intron Biotechnology, South Korea). Primers for the experiments were purchased from IDT, and their sequences of primers were as follows: *EMXI* FP; GGG TCA TAG GCT CTC TCA TTT AC, *EMXI* RP; CCA TTG CTT GTC CCT CTG T, Multiplex *EMXI* FP; CCA TTG CTT GTC CCT CTG T, Multiplex *EMXI* RP; CCA TTG CTT GTC CCT CTG T. The target region was amplified from 150 ng gDNA using the Q5 high-fidelity DNA polymerase (NEB, USA) and the specified primers. For the NHEJ and HDR samples, the PCR program consisted of an initial denaturation step at 98 °C for 30 s, followed by 30 cycles of denaturation at 98 °C for 10 s, annealing at 65 °C for 20 s, extension at 72 °C for 20 s, and a final extension at 72 °C for 2 m. The PCR program for the multiplex editing sample involved an additional extension step at 72 °C for 1 m. The final PCR product was purified using the Monarch PCR and DNA cleanup kit (NEB, USA).

T7E1 assay

The purified 200 ng PCR product was denatured at 95 °C for 5 m, followed by re-annealing through a two-step ramping process: first from 95 to 85 °C at a rate of 2 °C/s, and then from 85 to 25 °C at a rate of 0.1 °C/s. The resulting heteroduplexed PCR product was subjected to digestion at 37 °C for 15 m with 10 units of T7 endonuclease 1 (NEB, USA). Finally, the analysis was performed using 1.5% TBE agarose gel electrophoresis. DNA sample was loaded together with low molecular weight DNA ladder (NEB N3233S).

Restriction enzyme assay

For HDR analysis using restriction enzyme digestion, the 200 ng purified PCR product was incubated with 5 units of EcoRV-HF(NEB) in rCutSmart buffer at 37 °C. After 2 h, the reaction was stopped with heat inactivation at 65 °C for 20 min. The product was analyzed by electrophoresis using 1.5% TBE agarose gel.

NGS sample preparation

For targeted deep sequencing analysis, a DNA substrate was prepared by following the upper DNA substrate construction protocol using distinct primer sets: *EMXI* NGS FP; GCCTCCTGAGTTTCTCATCTG, *EMXI* NGS RP; CTAGTCATTGGAGGTGACATCG, Multiplex *EMXI* NGS FP; TCTGGAGCAAGAATCCAAGAG, Multiplex *EMXI* NGS RP; CTAGTCATTGGAGGTGACATCG. The resulting PCR product was purified using a Monarch PCR and DNA cleanup kit and subsequently subjected to deep sequencing analysis. The genomic sites of interest were amplified from genomic DNA samples and sequenced on a NovaSeq 6000 system (Illumina, USA).

High-speed microscopy, and image and data processing

High-speed images were recorded using a Phantom VEO 701 L high-speed camera (Vision Research, USA), and fluorescence images were captured using a standard inverted microscope (Axio Observer A1, Carl Zeiss, Germany). Both the high-speed and fluorescence images were analyzed using the ImageJ software (<https://imagej.nih.gov/ij/>). Guava flow cytometry data were analyzed using Guava software, Incyte 3.3.

Statistical analysis and reproducibility

For all experiments, at least three independent biological replicates were used unless otherwise noted. Statistical analysis was performed using a one-way ANOVA and Tukey's HSD post-hoc test for multiple comparisons using SPSS Statistics 27 (IBM, USA). A *P* value of < 0.05 was considered as statistically significant. All data were replotted using the OriginPro software (OriginLab, USA). Error bars and symbols in the plots represent the mean \pm standard error of the mean.

Confocal microscopy

Fluorescent-stained cells and internalized 3 kDa FITC were imaged using a confocal laser scanning microscope (Zeiss, Germany). The cells were fixed with 4% formaldehyde and stained with DAPI. Subsequently, the processed cells were affixed onto a poly-L-lysine (PLL)-coated glass slide covered with a mounting solution for confocal imaging.

Reporting summary

Further information on research design is available in the Nature Portfolio Reporting Summary linked to this article.

Data availability

All data generated or analyzed during this study are included in this published article and its supplementary information files. The NGS data generated in this study have been deposited in the NCBI Sequence Read Archive (SRA) under accession numbers [SRR28563326](https://www.ncbi.nlm.nih.gov/seq/submit/sra/), [SRR28563328](https://www.ncbi.nlm.nih.gov/seq/submit/sra/), and [SRR28563329](https://www.ncbi.nlm.nih.gov/seq/submit/sra/), associated with NCBI BioProject [PRJNA1096627](https://www.ncbi.nlm.nih.gov/bioproject/PRJNA1096627). Additionally, the GenBank accession number for the relevant sequences is [PP645754](https://www.ncbi.nlm.nih.gov/genbank/PP645754). All datasets are publicly accessible and will be permanently available, with no restrictions on data availability. Due to its size, the raw flow cytometry data is available upon request, and requests will be fulfilled within 2 weeks. Source data are provided with this paper.

References

- Gaj, T., Gersbach, C. A. & Barbas, C. F. 3rd. ZFN, TALEN, and CRISPR/Cas-based methods for genome engineering. *Trends Biotechnol* **31**, 397–405 (2013).

2. Gupta, R. M. & Musunuru, K. Expanding the genetic editing tool kit: ZFNs, TALENs, and CRISPR-Cas9. *J. Clin. Investig.* **124**, 4154–4161 (2014).
3. Doudna, J. A. & Charpentier, E. The new frontier of genome engineering with CRISPR-Cas9. *Science* **346**, 1258096 (2014).
4. Fajrial, A. K., He, Q. Q., Wirusanti, N. I., Slansky, J. E. & Ding, X. A review of emerging physical transfection methods for CRISPR/Cas9-mediated gene editing. *Theranostics* **10**, 5532–5549 (2020).
5. Rouet, R. et al. Receptor-Mediated Delivery of CRISPR-Cas9 endonuclease for cell-type-specific gene editing. *J. Am. Chem. Soc.* **140**, 6596–6603 (2018).
6. Kim, S., Kim, D., Cho, S. W., Kim, J. & Kim, J. S. Highly efficient RNA-guided genome editing in human cells via delivery of purified Cas9 ribonucleoproteins. *Genome Res.* **24**, 1012–1019 (2014).
7. Hughes, T. S. et al. Immunogenicity of intrathecal plasmid gene delivery: cytokine release and effects on transgene expression. *J. Gene. Med.* **11**, 782–790 (2009).
8. Yin, K., Gao, C. & Qiu, J.-L. Progress and prospects in plant genome editing. *Nat. Plants* **3**, 17107 (2017).
9. Liang, Z. et al. Efficient DNA-free genome editing of bread wheat using CRISPR/Cas9 ribonucleoprotein complexes. *Nat. Commun.* **8**, 14261 (2017).
10. Hendel, A. et al. Chemically modified guide RNAs enhance CRISPR-Cas genome editing in human primary cells. *Nat. Biotechnol.* **33**, 985–989 (2015).
11. Chen, G. et al. A biodegradable nanocapsule delivers a Cas9 ribonucleoprotein complex for in vivo genome editing. *Nat. Nanotechnol.* **14**, 974–980 (2019).
12. Zuris, J. A. et al. Cationic lipid-mediated delivery of proteins enables efficient protein-based genome editing in vitro and in vivo. *Nat. Biotechnol.* **33**, 73–80 (2015).
13. Yu, X. et al. Improved delivery of Cas9 protein/gRNA complexes using lipofectamine CRISPRMAX. *Biotechnol. Lett.* **38**, 919–929 (2016).
14. Yang, R. et al. Monoclonal cell line generation and CRISPR/Cas9 manipulation via single-cell electroporation. *Small* **14**, 1702495 (2018).
15. Sido, J. M. et al. Electro-mechanical transfection for non-viral primary immune cell engineering. *bioRxiv*, 2021.2010.2026.465897 (2021).
16. Suresh, B., Ramakrishna, S. & Kim, H. in *Eukaryotic Transcriptional and Post-transcriptional Gene Expression Regulation* (ed. Wajapeyee, N. & Gupta, R.), pp. 81–94 (Springer New York, 2017).
17. Boukany, P. E. et al. Nanochannel electroporation delivers precise amounts of biomolecules into living cells. *Nat. Nanotechnol.* **6**, 747–754 (2011).
18. Meaking, W. S., Edgerton, J., Wharton, C. W. & Meldrum, R. A. Electroporation-induced damage in mammalian cell DNA. *Biochim. Biophys. Acta, Gene Struct. Expression* **1264**, 357–362 (1995).
19. Stewart, M. P., Langer, R. & Jensen, K. F. Intracellular delivery by membrane disruption: mechanisms, strategies, and concepts. *Chem. Rev.* **118**, 7409–7531 (2018).
20. Sun, M. & Duan, X. Recent advances in micro/nanoscale intracellular delivery. *Nanotechnol. Precis. Eng. (NPE)* **3**, 18–31 (2019).
21. Hur, J. & Chung, A. J. Microfluidic and nanofluidic intracellular delivery. *Adv. Sci.* **8**, 2004595 (2021).
22. Deng, Y. et al. Intracellular Delivery of nanomaterials via an inertial microfluidic cell hydroporator. *Nano Lett.* **18**, 2705–2710 (2018).
23. Han, X. et al. CRISPR-Cas9 delivery to hard-to-transfect cells via membrane deformation. *Sci. Adv.* **1**, e1500454 (2015).
24. Yu, T. et al. Development of a microfluidic cell transfection device into gene-edited CAR T cell manufacturing workflow. *Lab Chip.* **23**, 4804–4820 (2023).
25. Sevenler, D. & Toner, M. High throughput intracellular delivery by viscoelastic mechanoporation. *Nat. Commun.* **15**, 115 (2024).
26. Ding, X. et al. High-throughput nuclear delivery and rapid expression of DNA via mechanical and electrical cell-membrane disruption. *Nat. Biomed. Eng.* **1**, 0039 (2017).
27. Joo, B., Hur, J., Kim, G.-B., Yun, S. G. & Chung, A. J. Highly efficient transfection of human primary T lymphocytes using droplet-enabled mechanoporation. *ACS Nano* **15**, 12888–12898 (2021).
28. Sharei, A. et al. A vector-free microfluidic platform for intracellular delivery. *Proc. Natl Acad. Sci. USA* **110**, 2082–2087 (2013).
29. Qiu, H.-Y., Ji, R.-J. & Zhang, Y. Current advances of CRISPR-Cas technology in cell therapy. *Cell Insight* **1**, 100067 (2022).
30. Hur, J. et al. Microfluidic cell stretching for highly effective gene delivery into hard-to-transfect primary cells. *ACS Nano* **14**, 15094–15106 (2020).
31. Liu, A. et al. Microfluidic generation of transient cell volume exchange for convectively driven intracellular delivery of large macromolecules. *Mater. Today* **21**, 703–712 (2018).
32. Szeto, G. L. et al. Microfluidic squeezing for intracellular antigen loading in polyclonal B-cells as cellular vaccines. *Sci. Rep.* **5**, 10276 (2015).
33. Utada, A. S., Fernandez-Nieves, A., Stone, H. A. & Weitz, D. A. Dripping to jetting transitions in coflowing liquid streams. *Phys. Rev. Lett.* **99**, 094502 (2007).
34. Jarrell, J. A. et al. Intracellular delivery of mRNA to human primary T cells with microfluidic vortex shedding. *Sci. Rep.* **9**, 3214 (2019).
35. Kang, G. et al. Intracellular nanomaterial delivery via spiral hydro-rotation. *ACS Nano* **14**, 3048–3058 (2020).
36. Hur, J. et al. Genetically stable and scalable nanoengineering of human primary T cells via cell mechanoporation. *Nano Lett.* **23**, 7341–7349 (2023).
37. Featherstone, C. & Jackson, S. P. DNA double-strand break repair. *Curr. Biol.* **9**, R759–R761 (1999).
38. Sentmanat, M. F., Peters, S. T., Florian, C. P., Connelly, J. P. & Pruett-Miller, S. M. A Survey of validation strategies for CRISPR-Cas9 editing. *Sci. Rep.* **8**, 888 (2018).
39. Liu, C., Zhang, L., Liu, H. & Cheng, K. Delivery strategies of the CRISPR-Cas9 gene-editing system for therapeutic applications. *J. Control. Release* **266**, 17–26 (2017).
40. Liu, M. et al. Methodologies for Improving HDR Efficiency. *Front. Genet.* **9** <https://doi.org/10.3389/fgene.2018.00691> (2019).
41. Komor, A. C., Kim, Y. B., Packer, M. S., Zuris, J. A. & Liu, D. R. Programmable editing of a target base in genomic DNA without double-stranded DNA cleavage. *Nature* **533**, 420–424 (2016).
42. Anzalone, A. V. et al. Search-and-replace genome editing without double-strand breaks or donor DNA. *Nature* **576**, 149–157 (2019).
43. Wolff, J. H. & Mikkelsen, J. G. Prime editing in hematopoietic stem cells—From ex vivo to in vivo CRISPR-based treatment of blood disorders. *Front. genome.* **5**. <https://doi.org/10.3389/fgene.2023.1148650> (2023)
44. Aghamoo, M. et al. High-throughput and dosage-controlled intracellular delivery of large cargos by an acoustic-electric microvortices platform. *Adv. Sci.* **9**, 2102021 (2022).

Acknowledgements

The authors thank Mr. H. S. Lee and all members of the Biomicrofluidics Laboratory at Korea University for useful discussions and Prof. I. Choi and Mr. H. Kim at the University of Seoul for their technical support. This study was supported by the National Research Foundation of Korea (NRF) grants funded by the Korean government (MSIT; Ministry of Science and ICT) (2021R1A2C2006224, RS-2023-00242443, and RS-2023-00218543, A.J.C.), Technological Innovation R&D Program (RS-2023-00262758, A.J.C.) funded by the Ministry of SMEs and Startups (MSS, Republic of Korea), and Materials/Parts Technology Development Program (20020278, A.J.C.) funded by the Ministry of Trade, Industry & Energy (MOTIE, Republic of Korea).

Author contributions

Y.-J.K. and A.J.C. conceived the research, contributed to the data analysis, and designed the experiments. Y.-J.K. conducted all microfluidics-associated experiments. D.Y.Y. and C.J. designed the CRISPR systems, and D.Y.Y. performed CRISPR analyses. Y.-J.K. and A.J.C. wrote the manuscript with input from all authors. All the authors discussed the results and contributed to the writing of the manuscript.

Competing interests

A.J.C. declares the following competing interest: A financial interest in MxT Biotech, which is commercializing the presented technology. The remaining authors declare no competing interests.

Additional information

Supplementary information The online version contains supplementary material available at <https://doi.org/10.1038/s41467-024-52493-1>.

Correspondence and requests for materials should be addressed to Cheulhee Jung or Aram J. Chung.

Peer review information *Nature Communications* thanks Qiang Sun, Dayong Yang and the other, anonymous, reviewer(s) for their contribution to the peer review of this work. A peer review file is available.

Reprints and permissions information is available at <http://www.nature.com/reprints>

Publisher's note Springer Nature remains neutral with regard to jurisdictional claims in published maps and institutional affiliations.

Open Access This article is licensed under a Creative Commons Attribution-NonCommercial-NoDerivatives 4.0 International License, which permits any non-commercial use, sharing, distribution and reproduction in any medium or format, as long as you give appropriate credit to the original author(s) and the source, provide a link to the Creative Commons licence, and indicate if you modified the licensed material. You do not have permission under this licence to share adapted material derived from this article or parts of it. The images or other third party material in this article are included in the article's Creative Commons licence, unless indicated otherwise in a credit line to the material. If material is not included in the article's Creative Commons licence and your intended use is not permitted by statutory regulation or exceeds the permitted use, you will need to obtain permission directly from the copyright holder. To view a copy of this licence, visit <http://creativecommons.org/licenses/by-nc-nd/4.0/>.

© The Author(s) 2024